Correspondence to:
P. Bolgiani,
pbolgian@ucm.es

Microburst Detection With the WRF Model: Effective Resolution and Forecasting Indices

Pedro Bolgiani[1] [ID], **Daniel Santos-Muñoz[1]** [ID], **Sergio Fernández-González[2]** [ID], **Mariano Sastre[1]** [ID], **Francisco Valero[1,3]** [ID], and **María Luisa Martín[3,4]** [ID]

[1]Department of Earth Physics and Astrophysics, Faculty of Physics, Complutense University of Madrid, Madrid, Spain, [2]State Meteorological Agency (AEMET), Santander, Spain, [3]Interdisciplinary Mathematics Institute, Complutense University of Madrid, Madrid, Spain, [4]Department of Applied Mathematics, Faculty of Computer Engineering, University of Valladolid, Valladolid, Spain

Abstract Microbursts are meteorological phenomena in the lower troposphere which can produce damaging surface winds and pose a severe risk to aircraft flying close to the ground. As these events usually span less than 4 km and 15 min, the spatiotemporal resolution is a challenge for numerical simulations. Although research of microburst using operative mesoscale models is scarce, the Weather Research and Forecasting (WRF) model has been used in the diagnosis of this phenomenon. In this paper, such model is used to simulate several microburst conducive days using two different boundary conditions. The energy spectra of the simulations are computed to evaluate the effective resolution of the model. The results are in line with previous studies and produce no notable differences among the boundary conditions. Nonetheless, the energy spectra show an overenergetic troposphere at microscale resolutions, rendering the effective resolution inadequate for microburst forecasting using the simulated physics variables. Thus, mesoscale indices are analyzed as a prognostic tool. The wind index, the wet microburst severity index and the microburst windspeed potential index do not show high forecasting performances, even though improving the results of climatology. Also, notable differences among the boundary conditions can be seen. The most consistent results are achieved by the wet microburst severity index.

1. Introduction

A *microburst* is a strong downdraft in the lower troposphere, generated by dynamic and thermodynamic effects in the midtroposphere, which produces a divergent pattern of surface wind with a differential speed of, at least, 20 m s^{-1} (Fujita, 1985; Fujita & Byers, 1977; Fujita & Wakimoto, 1981; Wakimoto, 1985). This surface wind forms a toroidal-shaped gust front (*outflow*) prone to producing severe damage, presenting a diameter under 4 km and a lifespan under 15 min (Fujita, 1980, 1981a). The differential wind speed over a relatively small distance produces a severe change in the relative airspeed of an aircraft flying through the outflow, posing a risk for aircraft flying low and slow, as in take off and landing operations. Being the event related to several accidents in the decade of 1980, microbursts are defined as a major meteorological hazard for aviation and flight safety (Fujita, 1980, 1981b; Wolfson et al., 1994). This promoted four major field campaigns, the latest one being the microburst and severe thunderstorm (MIST) project (Atkins & Wakimoto, 1991). Since these, no other major observational research has been performed specifically for microbursts, and thus, there is not much data based on adequate instruments. Srivastava (1987) performed notable studies in laboratory conditions to develop an ideal one-dimensional thermodynamic model, which was then confirmed by Doppler radar observations (Atlas et al., 2004). Proctor (1988) used ad hoc numerical models to gain further insight on the evaporative cooling of rain and hail, and on the dynamics of the outflow. This was later reproduced in idealized runs of numerical models (Lin et al., 2007; Vermeire et al., 2011), also used by James and Markowski (2010) to prove that dry air aloft is detrimental to microburst generation, contrary to previous findings. Some other ideal cloud models have been used for the research of downbursts (Oreskovic et al., 2018; Orf et al., 2012), but not particularly for microbursts. The review on aviation meteorology conducted by Gultepe et al. (2019) shows that research on the topic has been scarce in the last two decades, and that it still remains a very elusive phenomenon for prediction. To the authors' knowledge, the simulations performed by Bolgiani et al. (2020) are the first attempt to evaluate the ability of a mesoscale numerical weather prediction model to capture the characteristic variables of the microburst.

Microbursts can be divided in two categories considering the amount of precipitation generated and the radar reflectivity of the convective cell (Fujita, 1985; Fujita & Wakimoto, 1981; Wilson et al., 1984). Thus, *low-reflectivity* or *dry* microbursts generate less than 0.25 mm of precipitation and a reflectivity below 35 dBZ, while *high-reflectivity* or *wet* microbursts show values above those thresholds. High-reflectivity microbursts are associated with the development of convective cells (Atkins & Wakimoto, 1991), which occur at small spatiotemporal scales (Kunz, 2007), rendering the forecast a challenging task. In this regard, the use of thermodynamic indices can be very useful in the operation forecasting of extreme weather events (Gascón et al., 2015). Previous results by the authors show the ability of the Weather Research and Forecasting (WRF) numerical model to properly capture the variables and dynamics of the high-reflectivity microburst (Bolgiani et al., 2020). The vertical thermodynamic profile, the dimensions, and timing of the event are appropriately reproduced. The simulations show a descending reflectivity core which generates a precipitation shaft, associated with a vertical wind speed minimum and the related surface outflow. Surface and vertical wind speeds, reflectivity, precipitation, temperature lapse rate, and surface temperature are correctly reproduced as well, although a tendency to underestimate their intensity is observed. Nonetheless, the model presents a low sensitivity to the thermodynamic conditions, generating microbursts even when the simulated atmospheric environment is nonconducive to it. This casts doubts on the ability of the WRF model to properly forecast the phenomenon. In turn, the question arises as to whether using microscale spatial resolutions adds value to the simulations or simply forces the model to compute equations without retaining any useful data from the mesoscale and boundary conditions information.

This article is based on the aforementioned results and expands the previous research. The objectives of this study are two. First, to evaluate the effective resolution of the WRF model, used as an operational mesoscale model, in high spatiotemporal resolutions with two different boundary conditions. This is done to establish the ability of the model to forecast microburst events. The second objective is to evaluate different microburst forecasting indices currently used as operational tools. Accordingly, the paper is organized as follows: Section 2 describes the data used, the model configuration, the kinetic energy spectrum, and the microburst forecasting indices. Section 3 presents the assessment methods used, followed by the results and discussion in section 4. Finally, the conclusions are summarized in section 5.

2. Experiment Design

The experiment for this paper consists of the numerical simulation and assessment of two sets of simulations. Each set comprehends 20 days with recorded observations. The data used for validation are the observations of the MIST project (Atkins & Wakimoto, 1991), which is one of the major researches performed in microbursts. This field program was conducted in the northern part of the State of Alabama (USA) during June and July 1986, using a mesoscale array of 71 surface stations and three Doppler radar stations. A total of 62 microbursts are observed in 15 days, and 3 days are described as thunderstorm situations with no microbursts observations. All these days are simulated along with two others, which are randomly chosen among the remaining 43 days with no recorded microbursts nor special observations (Table 1).

2.1. WRF Configuration

The simulations are performed using the nonhydrostatic mesoscale Advanced Research WRF model version 4.0.3, which has been extensively proven and validated (Skamarock et al., 2008; Skamarock & Klemp, 2008). The configuration of the model is based on the best results from previous research by the authors on the same subject and study domain (Bolgiani et al., 2020). Four concentric domains (D1, D2, D3, and D4 from outermost to innermost) are defined with a two-way nesting strategy (Figure 1). The position and area of D4 approximately corresponds to the spatial domain of the MIST project (Atkins & Wakimoto, 1991), centered on 086°50″W 34°44″N. The resolution for each domain is as follows: D4 is 202 × 202 grid points with 400 m spatial and 3 min of output temporal resolution, D3 is 151 × 151 grid points with 1,200 m spatial and 30 min temporal resolution, D2 is 121 × 121 grid points with 3,600 m spatial and 60 min temporal resolution, and D1 is 121 × 121 grid points with 10,800 m spatial and 180 min temporal resolution. The vertical domain is 59 sigma levels from 1,000 to 50 hPa, with resolution decreasing with altitude, and four soil levels. Each day is simulated with a cold start run from 01:00 to 01:00 local time (LT) the next day. This allows for spin

Table 1
Dates Selected for Evaluation and Number of Microbursts Observed During the MIST Project

Date	Observation	Date	Observation	Date	Observation	Date	Observation
3 Jun	3	24 Jun	6	16 Jul	1	4 Jun	TH
7 Jun	6	26 Jun	2	17 Jul	1	10 Jun	TH
8 Jun	3	1 Jul	1	19 Jul	2	28 Jun	TH
17 Jun	5	6 Jul	4	20 Jul	1	10 Jul	NIL
21 Jun	1	13 Jul	25	28 Jul	1	23 Jul	NIL

Note: TH indicates observation of thunderstorms but no microburst, NIL indicates no special observation.

up, reaching the simulation daytime in stable conditions. Please note, LT is Universal Time Coordinated minus 5 hr for this time and location.

As per the parametrizations used, the microphysics scheme is Morrison (Morrison et al., 2009) and the planetary boundary layer (PBL) scheme is Mellor-Yamada-Janjic (Janjic, 1994). Longwave and shortwave radiation schemes are New Goddard called every 10 min (Chou et al., 2001; Chou & Suarez, 1999), soil layers scheme (technically, land surface scheme) is Unified Noah (Tewari et al., 2004), and surface-atmosphere interface scheme (technically, surface layer scheme) is Eta Similarity (Janjic, 1994). Cumulus clouds are computed for D3 and D4, while the Grell-Freitas Ensemble scheme called every time step (Grell & Freitas, 2014) is used for D1 and D2. The model is operated as nonhydrostatic in the four domains, with no w-damping. Please, refer to the data set associated with this paper for the complete model configuration details (see Data Availability Statement).

Two sets of simulations are performed, the only difference being in the boundary conditions used. One is taken from the Climate Forecast System Reanalysis (CFSR) developed by the National Centers for Environmental Prediction (NCEP). This has a surface spatial resolution of 0.312°, atmospheric spatial resolution of 0.5° and 37 vertical levels (Saha et al., 2010). The other conditions used are the European Centre for Medium-Range Weather Forecasts Re-Analysis 5 (ERA5), with a spatial resolution of 0.25° and 37 pressure levels (European Centre for Medium-Range Weather Forecast, 2019). In both cases, the boundary conditions are provided to the model at 6 hr intervals.

2.2. Kinetic Energy Spectrum and Model Resolution

Since the numerical simulation of meteorology became a widespread research tool, the increase of spatiotemporal resolutions has been one of the paradigms for improving models and forecasting. As the availability of computational power has made high resolutions possible, the question arose as to what point increasing the model resolution is productive. One simple method of evaluating the effective resolution is to produce a diagram of the kinetic energy spectrum of the model (Skamarock, 2004). The spectral decomposition of the simulated wind produces a curve of the kinetic energy dissipation of the model. When this is compared to the theoretical dissipation curves, the performance of the model can be evaluated. The observations by Nastrom and Gage (1985) confirm that the kinetic energy associated with lower wave numbers (k), namely the planetary and large-scale processes, follows a theoretical dissipation curve proportional to k^{-3}, while the mesoscale (<400 km) atmospheric energy dissipates proportional to $k^{-5/3}$ (Kolmogorov, 1941). These observations of the upper troposphere confirm the theoretical curves down to the microscale limit ($\approx$4 km) and are used by Lindborg (1999, equation 71) to create an equation which describes the energy dissipation. It has to be considered that the kinetic energy spectrum can be altered by synoptic conditions, the geographical region and even the local topography, thus, the domain selected for evaluation can induce
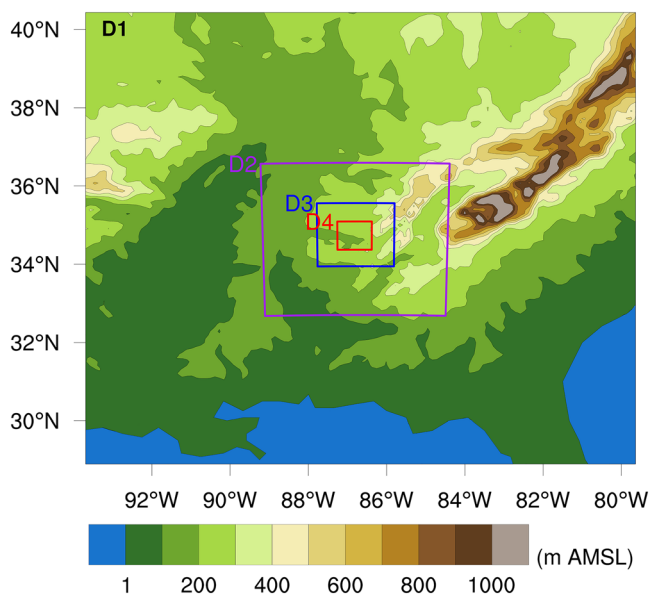

Figure 1. Orographic elevation and configuration of the nested domains used for the experiment.

differences in the spectrum curve (Ricard et al., 2013; Skamarock, 2004). On the other hand, it is not noticeably affected by the altitude selected (in the free troposphere) nor by the dimension in which the spectral decomposition is performed (latitude or longitude).

As evident as it may be, mesoscale models are not optimized for microscale events. In consequence, most of the parametrizations schemes are not designed for microscale grid resolutions, and they may limit the competence of the model in these simulations, for example, two-dimensional radiation schemes. Bolgiani et al. (2020) results yield that the model configuration used is able to properly reproduce the microburst, but show no sensitivity of the variables to the thermodynamic conditions conducive to the phenomenon. This may be related to the aforementioned inadequacy. In the case of kinetic energy, turbulence, and wind, the vast majority of operative mesoscale models lack a large eddy simulation process and simply parameterize the energy dissipation (Skamarock et al., 2008), rendering it an unreliable process at high frequencies. There is a limit where the model parameterizations cannot produce a realistic dissipation curve anymore, and the kinetic energy spectrum diverges from the observed curve; this marks the effective resolution of the model. Skamarock (2004) defines the effective resolution as the wavelength where the model's spectrum begins to decay relative to the observed spectrum. He also estimates it to be approximately seven times the grid resolution ($7\Delta x$) down to spatial resolutions of 4,000 m for the WRF model. Any resolution under this limit may be considered inadequate as per the kinetic energy simulated. Even more, the Nyquist-Shannon sampling theorem (Nyquist, 1928) states that to completely reproduce a certain frequency the sampling rate must be at least 2 times the frequency. Thus, the models filter out any wavelengths below $2\Delta x$, marking the minimum resolution (Skamarock & Klemp, 2008). Nevertheless, it is not clear that the model follows the same dissipation behavior as resolution is forced into microscale. In fact, these resolutions are named *terra incognita* by Wyngaard (2004) as they are too coarse for large eddy simulations and too small for the spatial filtering of the equations of motion. For the WRF model the threshold into terra incognita may be $\approx$1,400 m, as Rai et al. (2017) results show large variations of the wind speed field for higher resolutions. Notwithstanding, finer resolutions can be explored as a better resolved orography and land surface processes can improve the PBL modelization (Skamarock, 2004).

2.3. Microburst Forecasting Indices

The dimensions of the microbursts are a challenge for predictability, not only when using numerical models but also when using real time data. As per the state of the art, the most reliable technique today would be nowcasting high-reflectivity microbursts by observing the descent of the reflectivity core using a Doppler-radar (Roberts & Wilson, 1989). Apart from this, every other forecasting technique relies on mesoscale data; essentially, algorithms trying to condensate the thermodynamic situation conducive to a microburst. There are three principal ad hoc algorithms for microburst forecasting:

McCann (1994) introduced the wind index (WINDEX) as a dimensionless index based on the thermodynamic profiles observed in microburst situations. It is designed to be computed from a regular sounding (it can also be calculated from satellite soundings) and comprehends the data from the ground to the 0°C level, where the microbursts initiate. It is formulated as follows:

$$\text{WINDEX} = 2.572 \left[H_M \, R_Q \, \left(\Gamma^2 - 30 + Q_L - 2Q_M \right) \right]^{0.5} \tag{1}$$

where H_M is the height of the 0°C level in (km above the ground), $R_Q = Q_L/12$ but not greater than 1, Γ is the temperature lapse rate from the surface to the 0°C level (°C km^{-1}), Q_L is the average mixing ratio in the lowest 1 km above the surface (g kg^{-1}), and Q_M is the mixing ratio at the 0°C level (g kg^{-1}). Originally, the WINDEX is calibrated to yield a product equal to knots, but here the scaling factor is 2.572 to estimate the index in m s^{-1}. Typical values for this index would be the same as for the wind speed associated with the microburst.

Pryor and Ellrod (2004) produced the wet microburst severity index (WMSI). This dimensionless index considers convection to summarize the thermodynamic profile and precipitation formation, and the equivalent potential temperature deficit from the ground to the midtroposphere as an indicator of evaporative cooling and the generation of negative buoyancy. It is designed to be computed from satellite data. It is defined as follows:

$$WMSI = CAPE \, (\Theta e_{max} - \Theta e_{min})/1,000 \tag{2}$$

where CAPE is the surface based convective available potential energy (J kg^{-1}), Θe_{max} is the maximum value of equivalent potential temperature at the surface, and Θe_{min} is the minimum value of equivalent potential temperature in the midlevels of the troposphere. The scaling factor of 1,000 J kg^{-1} is applied based on observations. Typical values for this index would be ≈50 for a 18 m s^{-1} wind gust or 80 for a 26 m s^{-1} wind gust.

Pryor (2015) then developed the microburst windspeed potential index (MWPI). This is another dimensionless index, formulated as an improvement of the previous one. It considers updated knowledge on the role of relative humidity in the troposphere and is designed to consider both high and low reflectivity microbursts. It is composed as follows:

$$MWPI = CAPE/1,000 + \Gamma/5 + \left[(T - T_d)_{850} - (T - T_d)_{670} \right]/5 \tag{3}$$

where Γ is the temperature lapse rate from 850 to 670 hPa (°C km^{-1}), T is temperature (°C) and T_d is dewpoint temperature (°C), both at 850 and 670 hPa. The scaling factors of 1,000 J kg^{-1}, 5°C km^{-1} and 5°C are applied based on observations. Typical values for this index would be ≈2 for a 19 m s^{-1} wind gust or 4 for a 23 m s^{-1} wind gust.

Most of the data used to compute these products are derived from satellite instruments such as the Infrared Atmospheric Sounder Interferometer (Menzel et al., 2018), which provides a vertical resolution of 1 km in the lower troposphere, a horizontal resolution of 25 km, and an accuracy of 1 °K. This instrument is currently operating in polar orbiting satellites and is planned to be onboard the geostationary Meteosat Third Generation (Serio et al., 2012). As a consequence of the resolutions provided, none of these indices can produce a spatiotemporal accurate prognostic, although they are useful tools to identify meso-beta conditions.

3. Assessment Methodology

The software used to perform the evaluation are the R programming language (R Core Team, 2020) version 3.4.4 and the National Center for Atmospheric Research Command Language (NCAR, 2019) version 6.6.2. Please refer to the data set associated with this paper for the script details (see Data Availability Statement).

The methodology used for producing the kinetic energy spectrum is based on the procedure described by Skamarock (2004) and Abdalla et al. (2013). Wind speed is calculated (using *u*, *v*, and *w* components) at hourly intervals from 07:00 to 24:00 LT. This time window allows for a spin up time of 6 hr while spanning the complete diurnal variation of microbursts recorded by Atkins and Wakimoto (1991). The anomalies are computed by removing the average wind speed, and the time series is detrended before calculating the energy. The spectral decomposition of the energy is performed longitudinal-wise (at each latitudinal grid point) using single vertical (sigma) levels. The resulting energy spectra are averaged over latitude and then over every day simulated. Thus, hourly energy spectra for each set of simulations are derived. These are plotted together with the total average. The plots are redimensioned into wave number and energy density for easier understanding. The Lindborg (1999, equation 71) energy dissipation curve is added to ease the assessment. The wind speed at 1,000 hPa is selected for evaluation, as the closest level to the ground, where the microburst's outflow takes place. It is worth mentioning that, as we are evaluating the energy on a single level and a relatively small domain, the potential energy differences can be overlooked and the kinetic energy can be considered the total of the system.

To test the aforementioned microburst indices, a dichotomous validation is performed (Nurmi, 2003). This is computed using many thresholds for each index, thus assessing the sensitivity of the algorithm. As the observational data available (Atkins & Wakimoto, 1991) does not provide location or timing of the microbursts (only the number observed each day), the validation needs to be performed for the complete domain in daily time windows. To achieve this, the indices are calculated at every grid point for D2, D3, and D4, from 07:00 to 24:00 LT at each output time. To equate the assessment area, D2 and D3 are cropped to match D4. Considering that the microburst downdraft requires ≈10 min to reach the surface (Srivastava, 1987), and an average microburst outflow lifespan of 15 min (Hjelmfelt, 1988), the domain maxima are then selected every 30 min (as D2 has a temporal resolution of 60 min, results are linearly interpolated). This yields 34

maximum values for each index at each day. To create the daily contingency tables, a threshold is selected for the index in question, and any value reaching that threshold is considered a hit. When the number of hits does not reach the number of daily observations, the remainder are considered misses. When the daily hits exceed the number of observations, the surplus are considered false alarms. If there are no hits and no observations, a correct negative is considered. Following the previous procedure, contingency tables are computed for various threshold values: WINDEX from 0 to 29 at single-unit increases, WMSI from 0 to 290 at 10-unit increases, and MWPI from 0 to 14.5 at 0.5-unit increases. The resulting tables are used to calculate the probability of detection (POD) and probability of false detection (POFD) of each threshold and domain resolution. These are then averaged over every day creating a POD and a POFD for each index threshold considered, which can be compared in a receiver operating characteristic (ROC) curve plot. In addition, the area under the curve (AUC) for each index are computed (Nurmi, 2003) using a trapezoidal integration. Finally, to establish a reference for comparison, the climatology ROC curve is also plotted. The climatology is defined as the daily average from the summation of the three major microburst field programs (Atkins & Wakimoto, 1991; McCarthy et al., 1982; Wolfson et al., 1985), considering every day of study and conforming the data to the MIST domain area. Thus, the climatology results in an average of 1.5 microbursts per day in the MIST domain and a standard deviation (σ) of 3.7. The aforementioned procedure is followed to create the contingency tables for climatology, although in this case the thresholds are computed using $\pm 3\sigma$ increases from the average.

4. Results and Discussion

As the spectra are affected by the amount of energy in the system, before evaluating the overall energy spectrum for the simulations, it is worth to previously consider the response it shows to several factors. With this objective, different days at 18:00 LT are evaluated against the thermodynamic diagram and the synoptic situation in Figure 2. Three days are selected, each one representing a different situation: 6 July is a day with four microburst observations, 10 June is a day with thunderstorms but no microbursts observations, and 23 July is a typical summer day with no thunderstorm nor microburst observations. As the results are very similar for both boundary conditions, only those for ERA5 are shown, based on the better resolution provided by these conditions. The 6 July day presents a characteristic high-reflectivity microburst thermodynamic diagram associated with deep convection (Atkins & Wakimoto, 1991) and showing an almost superadiabatic dry layer below the cloud base (850 hPa). These mesoscale conditions are in contrast with the low energetic synoptic conditions, which show small pressure gradients and wind speeds for D1. Thus, the spectrum for D1 falls below the expected curve, in line with previous results (Ricard et al., 2013; Skamarock, 2004). It should also be considered that the theoretical curve (Lindborg, 1999) is estimated for the upper troposphere and these spectra are computed at 1,000 hPa. At finer resolutions, higher amounts of energy are captured by the model (Rai et al., 2017; Skamarock & Klemp, 2008), hence the parallel shifting to lower wavelengths in smaller domains, which can also be appreciated in Skamarock (2004) results. This is most evident for D4, which produces an unrealistically overenergized spectrum as a consequence of the model trying to resolve microscale winds affected by convection and orographic forcing. To illustrate this, the average wind speed over the D4 area is computed on 6 July at 18:00 LT. The results for each resolution are 1.25 m s^{-1} for 10,800 m, 1.28 m s^{-1} for 3,600 m, 1.30 m s^{-1} for 1,200 m, and 1.83 m s^{-1} for 400 m.

The 10 June day presents a more humid thermodynamic diagram with a deep conditionally unstable layer reaching above the 0°C level, at $\approx$600 hPa (Figure 2). The atmospheric pattern highlights an energetic situation, with a low-pressure system on the west generating a considerable gradient and wind speeds in agreement with a front passage. As a result, the dissipation curves are steeper and yield larger amounts of energy for every domain, most noticeable for D3. D4 yields an unrealistic result again and D1 comes closer to the expected curve, correcting the low-energy situation of 6 July but still penalized by the lower-energy content of near-surface winds. The results for 23 July show a low-energy stable atmospheric pattern with unstable local conditions. These are evident in the thermodynamic diagram and the wind speed "spots," probably generated by mesoscale convective systems. Thus, D1 and D2 present a somewhat mixed state between the previous two situations, while D3 shows a curve very similar to 6 July most probably due to local instability. These three spectra seem to converge into a general spectrum, as they also do for 6 July. Nevertheless, D4 is an outlier once more, generating an unrealistic level of energy, even this being the lowest of the three days evaluated.
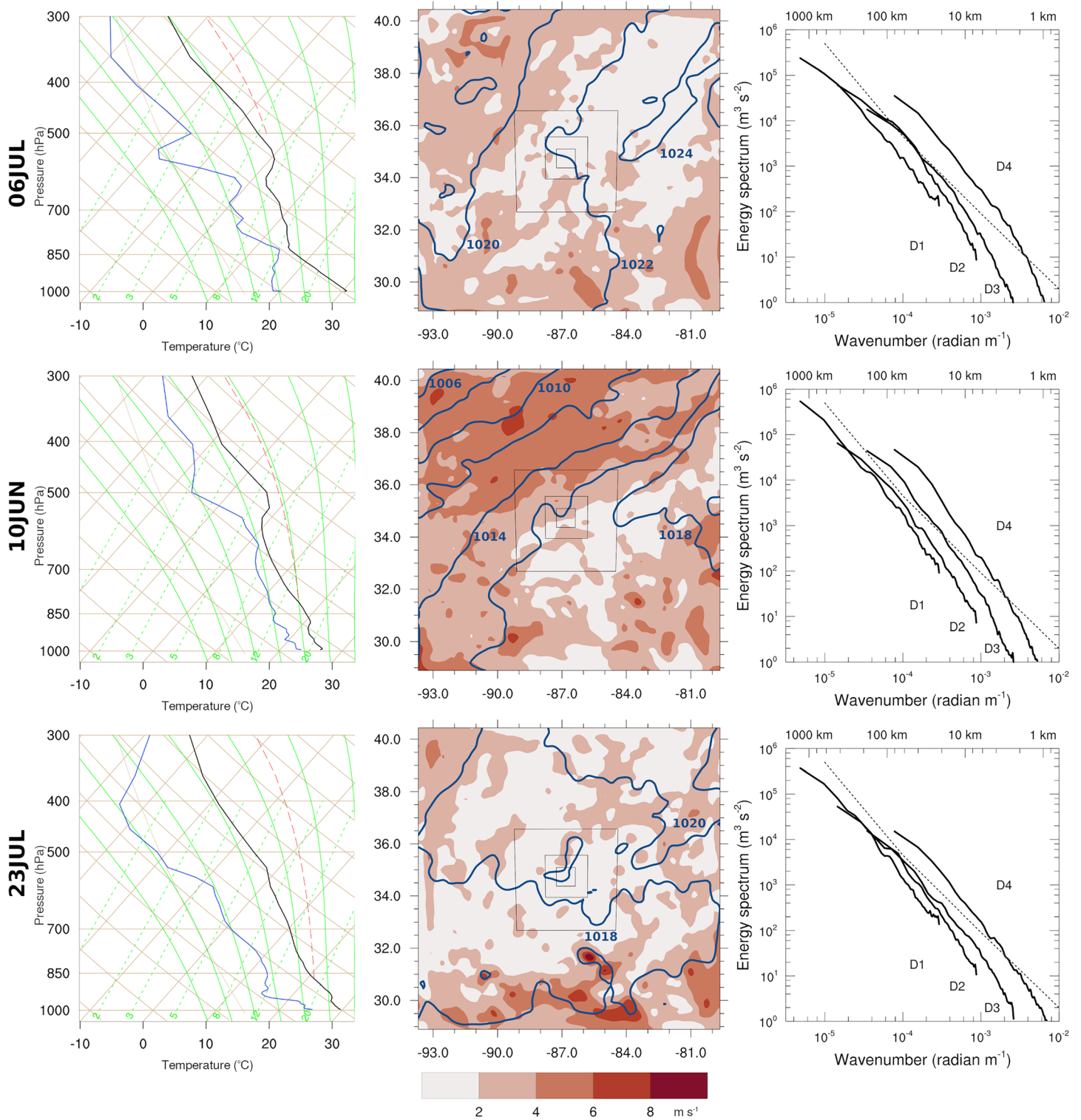
Figure 2. Synoptic analysis for ERA5 simulations at 18:00 LT for 6 Jul (four microbursts observed), 10 Jun (thunderstorms observed), and 23 Jul (no significant weather observed): (left column) Thermodynamic diagram at the center of the domain; black line is temperature, blue line is dew point temperature. (middle column) Sea level pressure (hPa) and wind speed at 1,000 hPa; black squares represent inner domains as per Figure 1. (right column) Wind kinetic energy spectra at 1,000 hPa; dashed line represents dissipation rates as per Lindborg (1999, equation 71).
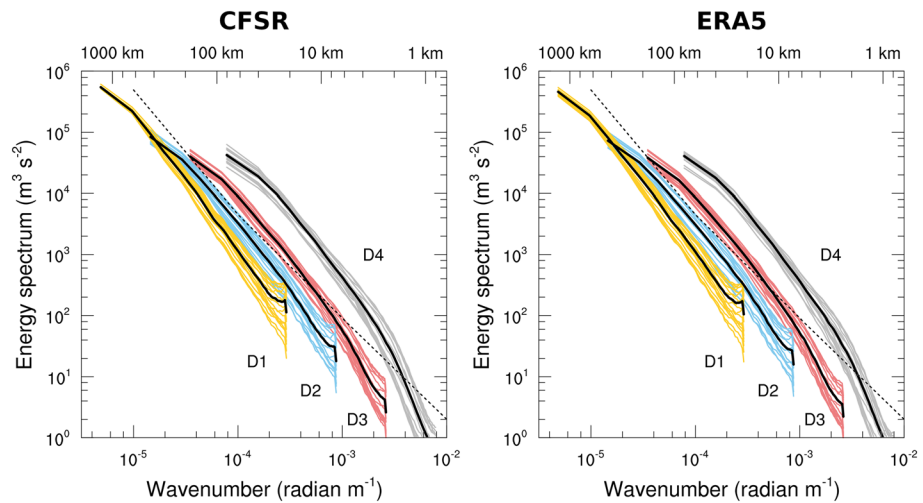
Figure 3. Wind kinetic energy spectra at 1,000 hPa for each domain and set of simulations: (left) CFSR; (right) ERA5. Black curves correspond to the spectral average. Dashed line corresponds to dissipation rates as per Lindborg (1999, equation 71).

4.1. Energy Spectrum

When evaluating the total average kinetic energy spectra for each set of simulations (Figure 3), the first results to consider are the differences among them. The spectra are very similar for CFSR and ERA5, although CFSR inputs a slightly larger amount of energy in the simulations, most noticeable in the smaller wave numbers at D1 and D2. This is consistent with the fact that both boundary conditions are taken from smooth reanalyses, which contribute little energy to the mesoscale spectrum. Nevertheless, the different energy content can also be appreciated in the mesoscale wave numbers, as the spin up time allows the energy to be transmitted downstream from large-scale wave numbers, generating fine-scale structures (Skamarock, 2004). Notwithstanding the previous considerations, the similarity of the spectra renders the influence of boundary conditions negligible. The maximum resolution of each spectra equals the domain size, as this acts as a filter for larger wavelengths. The decay of the curves when reaching the upper energy limits is related to the fact that they are computed at 1,000 hPa, removing the planetary-scale waves present in the upper troposphere (Skamarock, 2004). The minimum resolution for the curves follows the $2\Delta x$ rule as expected (Nyquist, 1928). The spectra also produce a decaying tail with a small upturn before the minimum resolution, proving only that a small aliasing of larger wave numbers is being generated, in accordance with the typical limited-area model behavior described by Skamarock (2004). The dispersion generated for each domain is created by the hourly spectra, and thus represents the average daily variability. As the majority of days simulated can be considered highly convective (Table 1), the variability is large and more pronounced in the smaller wavelengths. The convective activity is also responsible for part of the energy overestimation in the smaller wavelengths of the spectra. Nevertheless, similar to previous results, D4 produces a highly improbable overenergetic curve. In consequence, 400 m should be considered an unreliable resolution to simulate the meteorological conditions of the days selected. The same consideration should be done with the resolution of 1,200 m, as D3 also shows a large part of the curve above the expected energy level. This is consistent with the results of Rai et al. (2017) which establish the spatial resolution of 1,400 m as the beginning of terra incognita for the WRF model. On the other hand, the curve for D1 adjusts reasonably well to the expected dissipation rate for the larger wavelengths, as the energy deficit observed may be attributed to low-energy synoptic situations and the near-surface wind speeds. D2, with 3,600 m resolution, is the best performing domain. This is in line with the fact that WRF is a mesoscale model, not optimized to use microscale resolutions.

In addition, even if the spectra do not show a marked decay (Figure 3), an effective resolution can be established. A drop of the spectrum is clearly visible at a wavelength of ≈3 km for D4 and at ≈9 km for D3. The decay is still observable for D2 around 30 km. These effective resolutions are about $8\Delta x$, not far from the behavior described by Skamarock (2004). This has important implications for the simulation of
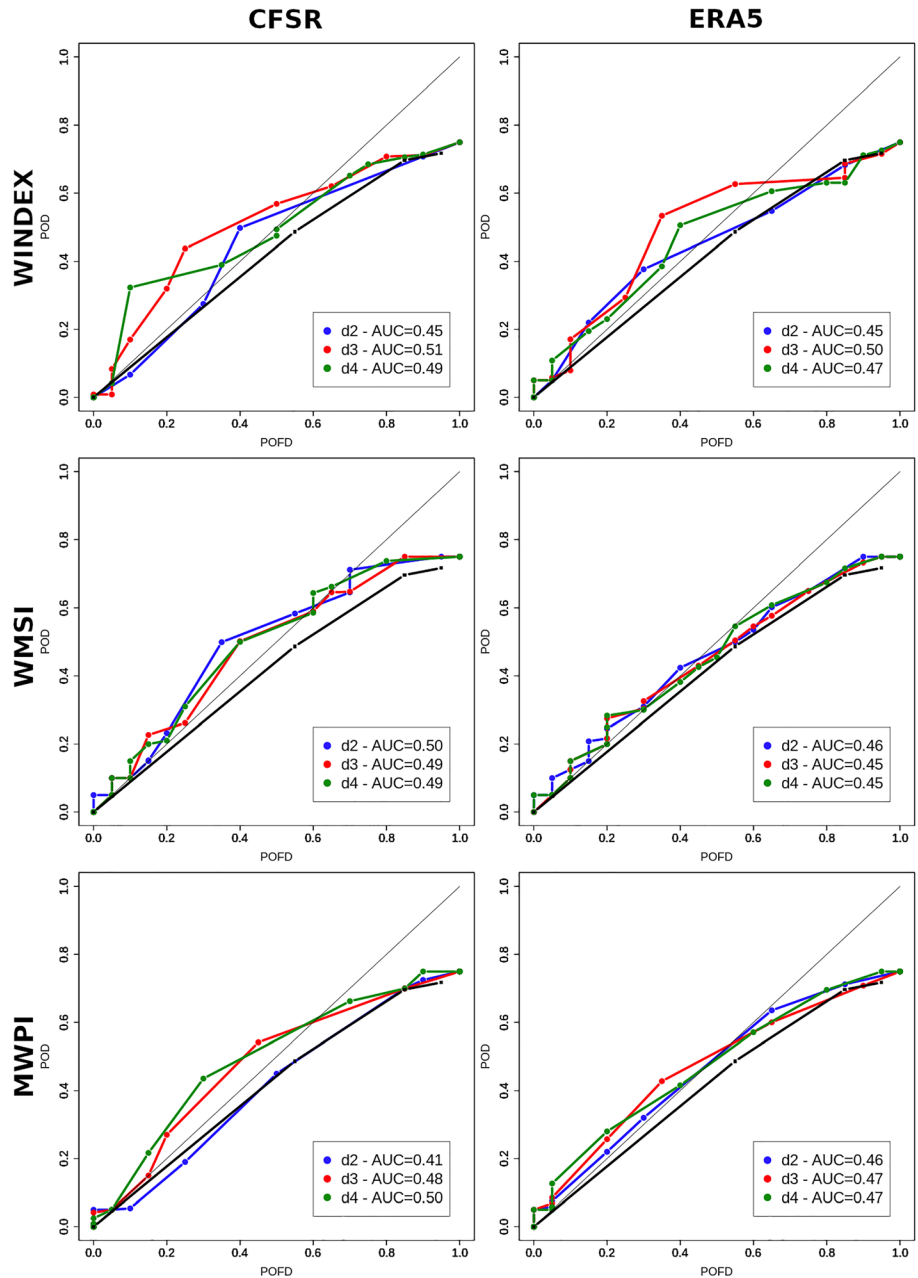
Figure 4. Average ROC curves and AUC for (top row) WINDEX, (middle row) WMSI, and (bottom row) MWPI tested at each domain and set of simulations: (left) CFSR; (right) ERA5. The black curve in each plot corresponds to the climatology ROC.

microbursts with WRF, as these cannot be considered appropriate resolutions for this kind of event. Bolgiani et al. (2020) results prove that the model is able to diagnose the microburst, properly simulating the characteristic variables and dynamics of the event, although when the physical variables' sensitivity are tested, they show no ability for forecasting. The results here produced for the energy spectrum are in line with these conclusions: as per the uncertainty introduced, no forecasting ability can be expected from the simulation of the microscale physical variables of a microburst. However, most of the variables considered by the microburst forecasting indices are mesoscale-related conditions (see section 2.3), therefore, these are worth to be evaluated.

4.2. Microburst Forecasting Indices

Figure 4 depicts the ROC curves for the three indices considered at both sets of simulations. Before evaluating the indices, it is worth analyzing the climatology curve. The forecast based on the climatological data yields a poor performance, even a negative predictive ability, as evident by a curve clearly below the nondiscrimination diagonal (this would represent a zero skill, random guess forecasting). These results are understandable when taking into account the large variability of the event, as highlighted by Table 1 and the first- and second-order moments of the climatology (1.5 and 3.7, respectively). In addition, as microbursts observations with the appropriate equipment are so scarce, the available climatological data yield a large uncertainty, making it a poor forecasting tool. Another feature to take into account is the behavior of the curve when reaching the maximum POFD. The curve reaches an inflection point, rapidly increasing the POFD for marginal increases of POD, which may be related to the contingency table for 13 July, as on this date 25 microbursts are observed. When the threshold used to compute the contingency table is decreased to a minimum, with the objective of reaching the 25 hits on this date, the number of false alarms rises dramatically for every other date. Thus, the average POFD reaches the maximum value before reaching a POD of 0.8. This feature is reproduced in every other curve in the figure.

When the ROC curves for the indices are evaluated (Figure 4), the results show that every one of them improves the results of the climatology forecast. Nevertheless, none shows an outstanding performance as no curve largely separates from the diagonal. Also, AUC values are hindered by the aforementioned inflection near the maximum POFD. Comparing the results for each boundary condition, CFSR performs better than ERA5 at every index. Even if the total energetic input is practically the same for both, that energy may be distributed in dissimilar spatial patterns or atmospheric variables. These variations will yield different energy expressions when downscaled and, in turn, the model will compute different values for a given variable. This effect is stronger for variables which are postprocessed from simpler ones, like CAPE or convection triggering. Although the different indices' results are not optimal, there is a clear added value against the climatology for the CFSR simulations. For the ERA5 set, only the WINDEX shows a forecasting ability (with slightly worse AUC than for CFSR), the WMSI and the MWPI being close to a random forecast.

Regarding the results for the CFSR (Figure 4), the WMSI yields the most robust ones, as every domain produces a similar curve with a maximum around 0.50 POD and 0.35 POFD. The AUC values reflect the same behavior, with very consistent results close to 0.49. The WINDEX at D3 produces the best AUC (0.51), nonetheless, each domain generates a different curve reflecting a less coherent forecast. The MWPI shows similar curves for D3 and D4, although D2 is a very poor performer, close to the climatology. The differences shown by the indices are in part related to the variables they consider and the complexity of the algorithm. This is evident for WINDEX, which presents a large variability among the different resolutions as it contemplates variables verging the microscale. The WMSI, on the other hand, only accounts for CAPE and Θe, which are variables indicative of the mesoscale behavior. It also may be tempting to conclude that the WINDEX at D3 presents the best AUC and therefore is the best performer, but here the energy spectrum results should be taken into account. The uncertainty and the effective resolution produced by microscale grid resolutions demand to take with care any other result on these domains and give priority to the most consistent ones.

5. Conclusions

In this study, several days with observed microbursts activity are simulated using the WRF model at high spatiotemporal resolutions and two different boundary conditions. The energy spectra of the simulations are evaluated to establish the minimum and effective resolutions of the model. These prompt the use of mesoscale forecasting indices for microbursts. According to the results, we can yield the following conclusions:

1. The kinetic energy quantity and dissipation rate simulated by the WRF model responds adequately to the different large-scale and mesoscale conditions evaluated.
2. The total input of energy by the CFSR and ERA5 reanalyses is practically identical.
3. The energy spectra fit reasonably well the observations in meso-beta resolutions. Nonetheless, when the model is forced into finer resolutions it produces an overenergetic troposphere.

4. Due to the unrealistic energy spectrum, the resolutions of 400 m (D4) and 1,200 m (D3) should be considered unreliable. Thus, considering the grid spacing of 3,600 m (D2), the minimum resolution for the simulations is 7.2 km and the effective resolution is approximately 30 km.

5. As per the aforementioned conclusion, the WRF simulation of microbursts is not reliable in atmospheric energy terms. This would partly explain the poor sensitivity of the characteristic variables shown by the authors in previous results (Bolgiani et al., 2020).

6. The forecasting ability of microburst climatology is very poor, most probably due to the very rare scientific observations.

7. When microburst forecasting indices based on mesoscale variables are applied, these show an improvement over a prognostic based on climatology.

8. CFSR boundary conditions show better prognostic results for the forecasting indices than ERA5.

9. The WMSI produces the most robust results, consistently achieving a POD of 0.50 against a POFD of 0.35 for every domain evaluated. Nevertheless, the WINDEX and the MWPI indices yield similar AUC values in some domains.

In summary, it can be concluded that the WRF model performs an adequate diagnosis of the microburst, although it does not present a high performance in the forecasting of the event. Nevertheless, the results show an added value over statistical data, indicating that it may be viable to achieve a reliable forecasting tool. Further research is required to improve the microburst detection using the WRF model, by fine-tuning the parametrizations, the model configuration, or developing new forecasting indices adapted to mesoscale numerical simulations.

Data Availability Statement

The model configuration files, data processing scripts, and processed data used to support the conclusions of this paper are available for further examination (https://doi.org/10.17632/fv6tg9n2jh.1).

References

Abdalla, S., Isaksen, L., Janssen, P., & Wedi, N. (2013). Effective spectral resolution of ECMWF atmospheric forecast models. *ECMWF Newsletter*, *137*, 19–22. https://doi.org/10.21957/rue4o7ac

Atkins, N. T., & Wakimoto, R. M. (1991). Wet microburst activity over the Southeastern United States: Implications for forecasting. *Weather and Forecasting*, *6*(4), 470–482. https://doi.org/10.1175/1520-0434(1991)006<0470:WMAOTS>2.0.CO;2

Atlas, D., Ulbrich, C. W., & Williams, C. R. (2004). Physical origin of a wet microburst: Observations and theory. *Journal of the Atmospheric Sciences*, *61*(10), 1186–1195. https://doi.org/10.1175/1520-0469(2004)061<1186:POOAWM>2.0.CO;2

Bolgiani, P., Fernández-González, S., Valero, F., Merino, A., García-Ortega, E., Sánchez, J. L., & Martín, M. L. (2020). Simulation of atmospheric microbursts using a numerical mesoscale model at high spatiotemporal resolution. *Journal of Geophysical Research: Atmospheres*, *125*, 1–23. https://doi.org/10.1029/2019JD031791

Chou, M., & Suarez, M. (1999). A solar radiation parameterization (CLIRAD-SW) for atmospheric studies. In *NASA Tech. Memo* (Vol. 10460).

Chou, M., Suarez, M., Liang, X., & Yan, M. (2001). A thermal infrared radiation parameterization for atmospheric studies. In *NASA Technical Report* (Vol. 19, Issue May 2003).

European Centre for Medium-Range Weather Forecast. (2019). ERA5 reanalysis (0.25 degree latitude-longitude grid). https://doi.org/10.5065/BH6N-5N20.

Fujita, T. T. (1980). Downbursts and microbursts, an aviation hazard. *19th Conference on Radar Meteorology*, 8.

Fujita, T. T. (1981a). Tornadoes and downbursts in the context of generalized planetary scales. *Journal of the Atmospheric Sciences*, *38*(8), 1511–1534. https://doi.org/10.1175/1520-0469(1981)038<1511:TADITC>2.0.CO;2

Fujita, T. T. (1981b). Microbursts as an aviation wind shear hazard. *19th Aerospace Sciences Meeting*, 9.

Fujita, T. T. (1985). In *The downburst: Microburst and macroburst*, *SMRP Research Papers* (Vol. 210, pp. 1–128). Chicago, Illinois, USA: University of Chicago.

Fujita, T. T., & Byers, H. R. (1977). Spearhead echo and downburst in the crash of an airliner. *Monthly Weather Review*, *105*(2), 129–146. https://doi.org/10.1175/1520-0493(1977)105<0129:seadit>2.0.co;2

Fujita, T. T., & Wakimoto, R. M. (1981). Five scales of airflow associated with a series of downbursts on July 16, 1980. *Monthly Weather Review*, *109*(7), 1438–1456. https://doi.org/10.1175/1520-0493(1981)109<1438:FSOAAW>2.0.CO;2

Gascón, E., Merino, A., Sánchez, J. L., Fernández-González, S., García-Ortega, E., López, L., & Hermida, L. (2015). Spatial distribution of thermodynamic conditions of severe storms in southwestern Europe. *Atmospheric Research*, *164-165*, 194–209. https://doi.org/10.1016/j.atmosres.2015.05.012

Grell, G., & Freitas, S. R. (2014). A scale and aerosol aware stochastic convective parameterization for weather and air quality modeling. *Atmospheric Chemistry and Physics*, *14*(10), 5233–5250. https://doi.org/10.5194/acp-14-5233-2014

Gultepe, I., Sharman, R., Williams, P. D., Zhou, B., Ellrod, G. P., Minnis, P., et al. (2019). A review of high impact weather for aviation meteorology. *Pure and Applied Geophysics*, *176*(5), 1869–1921. https://doi.org/10.1007/s00024-019-02168-6

Hjelmfelt, M. R. (1988). Structure and life cycle of microburst outflows observed in Colorado. *Journal of Applied Meteorology*, *27*(8), 900–927. https://doi.org/10.1175/1520-0450(1988)027<0900:SALCOM>2.0.CO;2

James, R. P., & Markowski, P. M. (2010). A numerical investigation of the effects of dry air aloft on deep convection. *Monthly Weather Review*, *138*(1), 140–161. https://doi.org/10.1175/2009MWR3018.1

Janjic, Z. I. (1994). The step-mountain eta coordinate model: Further developments of the convection, viscous sublayer, and turbulence closure schemes. *Monthly Weather Review*, *122*(5), 927–945. https://doi.org/10.1175/1520-0493(1994)122<0927:TSMECM>2.0.CO;2

Kolmogorov, A. N. (1941). The local structure of turbulence in incompressible viscous fluid for very large Reynolds numbers. *Doklady Akademii Nauk*, *434*(1890), 9–13. https://doi.org/10.1098/rspa.1991.0075

Kunz, M. (2007). The skill of convective parameters and indices to predict isolated and severe thunderstorms. *Natural Hazards and Earth System Sciences*, *7*(2), 327–342. www.nat-hazards-earth-syst-sci.net/7/327/2007/, https://doi.org/10.5194/nhess-7-327-2007

Lin, W. E., Orf, L. G., Savory, E., & Novacco, C. (2007). Proposed large-scale modelling of the transient features of a downburst outflow. *Wind and Structures, An International Journal*, *10*(4), 315–346. https://doi.org/10.12989/was.2007.10.4.315

Lindborg, E. (1999). Can the atmospheric kinetic energy spectrum be explained by two-dimensional turbulence? *Journal of Fluid Mechanics*, *388*, 259–288. https://doi.org/10.1017/S0022112099004851

McCann, D. W. (1994). WINDEX—A new index for forecasting microburst potential. *Weather & Forecasting*, *9*(4), 532–541. https://doi.org/10.1175/1520-0434(1994)009<0532:WNIFFM>2.0.CO;2

McCarthy, J., Wilson, J. W., & Fujita, T. T. (1982). The joint airport weather studies project. *Bulletin of the American Meteorological Society*, *63*(1), 15–22. https://doi.org/10.1175/1520-0477(1982)063<0015:TJAWSP>2.0.CO;2

Menzel, W. P., Schmit, T. J., Zhang, P., & Li, J. (2018). Satellite-based atmospheric infrared sounder development and applications. *Bulletin of the American Meteorological Society*, *99*(3), 583–603. https://doi.org/10.1175/BAMS-D-16-0293.1

Morrison, H., Thompson, G., & Tatarskii, V. (2009). Impact of cloud microphysics on the development of trailing stratiform precipitation in a simulated squall line: Comparison of one- and two-moment schemes. *Monthly Weather Review*, *137*(3), 991–1007. https://doi.org/10.1175/2008MWR2556.1

Nastrom, G. D., & Gage, K. S. (1985). A climatology of atmospheric wavenumber spectra of wind and temperature observed by commercial aircraft. *Journal of the Atmospheric Sciences*, *42*(9), 950–960. https://doi.org/10.1175/1520-0469(1985)042<0950:ACOAWS>2.0.CO;2

NCAR. (2019). NCAR command language (6.6.2). UCAR/NCAR/CISL/TDD. https://doi.org/10.5065/D6WD3XH5

Nurmi, P. (2003). Recommendations on the verification of local weather forecasts. In *ECMWF Technical Memorand*. https://doi.org/10.21957/y1z1thg5l

Nyquist, H. (1928). Certain topics in telegraph transmission theory. *Transactions of the American Institute of Electrical Engineers*, *47*(2), 617–644. https://doi.org/10.1109/T-AIEE.1928.5055024

Oreskovic, C., Orf, L. G., & Savory, E. (2018). A parametric study of downbursts using a full-scale cooling source model. *Journal of Wind Engineering and Industrial Aerodynamics*, *180*, 168–181. https://doi.org/10.1016/j.jweia.2018.07.020

Orf, L., Kantor, E., & Savory, E. (2012). Simulation of a downburst-producing thunderstorm using a very high-resolution three-dimensional cloud model. *Journal of Wind Engineering and Industrial Aerodynamics*, *104-106*, 547–557. https://doi.org/10.1016/j.jweia.2012.02.020

Proctor, F. H. (1988). Numerical simulations of an isolated microburst. Part I: Dynamics and structure. *Journal of the Atmospheric Sciences*, *45*(21), 3137–3160. https://doi.org/10.1175/1520-0469(1988)045<3137:NSOAIM>2.0.CO;2

Pryor, K. L. (2015). Progress and developments of downburst prediction applications of GOES. *Weather and Forecasting*, *30*(5), 1182–1200. https://doi.org/10.1175/WAF-D-14-00106.1

Pryor, K. L., & Ellrod, G. P. (2004). WMSI—A new index for forecasting wet microburst severity. *National Weather Association Electronic Journal of Operational Meteorology*, *25*, ■■■. http://citeseerx.ist.psu.edu/viewdoc/download?doi=10.1.1.510.9871&rep=rep1&type=pdf

R Core Team. (2020). R: Language and environment for statistical computing (3.4.4). R Foundation for Statistical Computing. https://www.r-project.org

Rai, R. K., Berg, L. K., Kosović, B., Mirocha, J. D., Pekour, M. S., & Shaw, W. J. (2017). Comparison of measured and numerically simulated turbulence statistics in a convective boundary layer over complex terrain. *Boundary-Layer Meteorology*, *163*(1), 69–89. https://doi.org/10.1007/s10546-016-0217-y

Ricard, D., Lac, C., Riette, S., Legrand, R., & Mary, A. (2013). Kinetic energy spectra characteristics of two convection-permitting limited-area models AROME and meso-NH. *Quarterly Journal of the Royal Meteorological Society*, *139*(674), 1327–1341. https://doi.org/10.1002/qj.2025

Roberts, R. D., & Wilson, J. W. (1989). A proposed microburst nowcasting procedure using single-Doppler radar. *Journal of Applied Meteorology*, *28*(4), 285–303. https://doi.org/10.1175/1520-0450(1989)028<0285:APMNPU>2.0.CO;2

Saha, S., Nadiga, S., Thiaw, C., Wang, J., Wang, W., Zhang, Q., et al. (2010). NCEP climate forecast system reanalysis (CFSR) 6-hourly products, January 1979 to December 2010. Research Data Archive at the National Center for Atmospheric Research, Computational and Information Systems Laboratory. https://doi.org/10.5065/D69K487J

Serio, C., Amoroso, M., Masiello, G., Venafra, S., Calbet, X., Stuhlmann, R., et al. (2012). Expected profiling retrieval performance of the Meteosat Third Generation infrared sounder. In D. Cimini, P. Di Girolamo, F. S. Marzano, & V. Rizi (Eds.), *Proceedings of the 9th International Symposium on Tropospheric Profiling*. L'Aquila, Italy: CETEMPS. http://cetemps.aquila.infn.it/istp/proceedings/

Skamarock, W. C. (2004). Evaluating mesoscale NWP models using kinetic energy spectra. *Monthly Weather Review*, *132*(12), 3019–3032. https://doi.org/10.1175/MWR2830.1

Skamarock, W. C., & Klemp, J. B. (2008). A time-split nonhydrostatic atmospheric model for weather research and forecasting applications. *Journal of Computational Physics*, *227*(7), 3465–3485. https://doi.org/10.1016/j.jcp.2007.01.037

Skamarock, W. C., Klemp, J. B., Dudhia, J., Gill, D. O., Barker, D. M., Duda, M. G., et al. (2008). A description of the advanced research WRF version 3. In *Technical Report*. https://doi.org/10.5065/D6DZ069T

Srivastava, R. C. (1987). A model of intense downdrafts driven by the melting and evaporation of precipitation. *Journal of the Atmospheric Sciences*, *44*(13), 1752–1774. https://doi.org/10.1175/1520-0469(1987)044<1752:AMOIDD>2.0.CO;2

Tewari, M., Chen, F., Wang, W., Dudhia, J., LeMone, M. A., Mitchell, K., et al. (2004). Implementation and verification of the unified NOAH land surface model in the WRF model. 20th Conference on Weather Analysis and Forecasting/16th Conference on Numerical Weather Prediction, 10–15.

Vermeire, B. C., Orf, L. G., & Savory, E. (2011). Improved modelling of downburst outflows for wind engineering applications using a cooling source approach. *Journal of Wind Engineering and Industrial Aerodynamics*, *99*(8), 801–814. https://doi.org/10.1016/j.jweia.2011.03.003

Wakimoto, R. M. (1985). Forecasting dry microburst activity over the high plains. *Monthly Weather Review*, *113*(7), 1131–1143. https://doi.org/10.1175/1520-0493(1985)113<1131:FDMAOT>2.0.CO;2

Wilson, J. W., Roberts, R. D., Kessinger, C. J., & McCarthy, J. (1984). Microburst wind structure and evaluation of Doppler radar for airport wind shear detection. *Journal of Climate & Applied Meteorology*, *23*(6), 898–915. https://doi.org/10.1175/1520-0450(1984)023<0898:MWSAEO>2.0.CO;2

Wolfson, M. M., Delanoy, R. L., Forman, B. E., Hallowell, R. G., Pawlak, M. L., & Smith, P. D. (1994). Automated microburst wind-shear prediction. *The Lincoln Laboratory Journal*, *7*(2), 399–426.

Wolfson, M. M., DiStefano, J. T., & Fujita, T. T. (1985). Low-altitude wind shear in the Memphis, TN area based on mesonet and LLWAS data. 14th Conference on Severe Local Storms, 322–327.

Wyngaard, J. C. (2004). Toward numerical modeling in the "Terra Incognita." *Journal of the Atmospheric Sciences*, *61*(14), 1816–1826. https://doi.org/10.1175/1520-0469(2004)061<1816:TNMITT>2.0.CO;2